Macromolecules

Article

Determining the Effective Density and Stabilizer Layer Thickness of Sterically Stabilized Nanoparticles

Bernice Akpinar,[†] Lee A. Fielding,*,[†,‡] Victoria J. Cunningham,[†] Yin Ning,[†] Oleksandr O. Mykhaylyk,[†] Patrick W. Fowler,[†] and Steven P. Armes*,[†]

[†]Department of Chemistry, University of Sheffield, Brook Hill, Sheffield, South Yorkshire S3 7HF, U.K.
[‡]School of Materials, The University of Manchester, Oxford Road, Manchester, M13 9PL, U.K.

Ⓢ *Supporting Information*

ABSTRACT: A series of model sterically stabilized diblock copolymer nanoparticles has been designed to aid the development of analytical protocols in order to determine two key parameters: the effective particle density and the steric stabilizer layer thickness. The former parameter is essential for high resolution particle size analysis based on analytical (ultra)centrifugation techniques (e.g., disk centrifuge photo-sedimentometry, DCP), whereas the latter parameter is of fundamental importance in determining the effectiveness of steric stabilization as a colloid stability mechanism. The diblock copolymer nanoparticles were prepared via polymerization-induced self-assembly (PISA) using RAFT aqueous emulsion polymerization: this approach affords relatively narrow particle size distributions and enables the mean particle diameter and the stabilizer layer thickness to be adjusted independently via systematic variation of the mean degree of polymerization of the hydrophobic and hydrophilic blocks, respectively. The hydrophobic core-forming block was poly(2,2,2-trifluoroethyl methacrylate) [PTFEMA], which was selected for its relatively high density. The hydrophilic stabilizer block was poly(glycerol monomethacrylate) [PGMA], which is a well-known non-ionic polymer that remains water-soluble over a wide range of temperatures. Four series of $PGMA_x-PTFEMA_y$ nanoparticles were prepared ($x = 28, 43, 63,$ and $98, y = 100-1400$) and characterized via transmission electron microscopy (TEM), dynamic light scattering (DLS), and small-angle X-ray scattering (SAXS). It was found that the degree of polymerization of both the PGMA stabilizer and core-forming PTFEMA had a strong influence on the mean particle diameter, which ranged from 20 to 250 nm. Furthermore, SAXS was used to determine radii of gyration of 1.46 to 2.69 nm for the solvated PGMA stabilizer blocks. Thus, the mean effective density of these sterically stabilized particles was calculated and determined to lie between 1.19 g cm⁻³ for the smaller particles and 1.41 g cm⁻³ for the larger particles; these values are significantly lower than the solid-state density of PTFEMA (1.47 g cm⁻³). Since analytical centrifugation requires the density *difference* between the particles and the aqueous phase, determining the effective particle density is clearly vital for obtaining reliable particle size distributions. Furthermore, selected DCP data were recalculated by taking into account the inherent density *distribution* superimposed on the particle size distribution. Consequently, the true particle size distributions were found to be somewhat narrower than those calculated using an erroneous single density value, with smaller particles being particularly sensitive to this artifact.
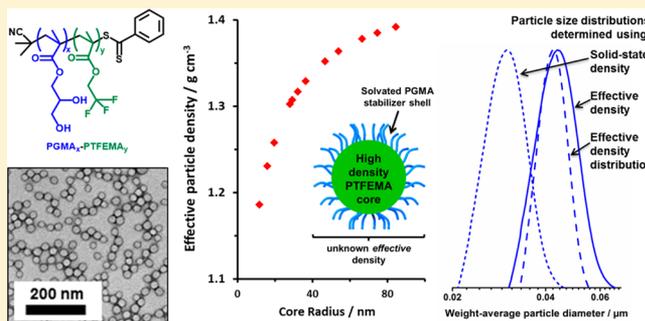
INTRODUCTION

Steric stabilization is widely recognized to be the most important mechanism for achieving long-term colloidal stability.[1,2] Unlike charge stabilization,[3] it confers thermodynamic stability at relatively high solids, is tolerant of added salt in aqueous formulations,[4] and can be designed for a wide range of media, including both polar solvents[5−11] and non-polar solvents[12−21] as well as more exotic solvents such as supercritical carbon dioxide[22−27] or ionic liquids.[28,29] In view of these many advantages, steric stabilization is now used on an industrial scale across a wide range of commercial sectors. Examples include the manufacture of copolymer latex paints,[12,30] ceramic dispersions,[31−35] ink formulations,[36] and antiwear additives for engine oils.[37−39] Steric stabilization is also

known to be a highly effective mechanism for preventing the biofouling of surfaces[40−45] and is important in determining the interfacial adsorption of particles[46] as well as the emulsion type for Pickering emulsifiers.[47]

The *effective particle density* and the *stabilizer layer thickness* are key parameters for sterically stabilized particles. Knowledge of the former parameter is vital for high resolution particle size analysis based on analytical (ultra)centrifugation.[48−50] This is because the density difference between the particles and the continuous phase is one of three primary variables, along with

the particle size and colloidal stability, that determine the rate of sedimentation (and hence the degree of particle fractionation). The latter parameter is of fundamental interest and is directly related to the observed colloidal stability, since it precisely determines the interparticle separation distance at which the steric repulsive term becomes important.[2] In principle, small-angle neutron scattering (SANS) can be used to determine the segment density profile of stabilizer chains normal to the particle surface and hence the mean stabilizer layer thickness. However, this sophisticated technique usually requires deuterated polymers for the contrast variation approach that yields the highest-quality data, but unfortunately such polymers are typically not available for most commercial systems of interest. Similarly, small-angle X-ray scattering (SAXS) can be used to determine stabilizer layer thicknesses. For example, Ballauff and co-workers have used SAXS to determine the stabilizer thickness for poly(ethylene oxide)-stabilized polystyrene (PEO−PS) latexes with core diameters ranging between 70 and 146 nm.[51,52] However, the problem of effective particle density was not considered. Moreover, this PEO−PS system is ill-suited to addressing this question because the density difference between the PS core and water (∼0.05 g cm^{-3}) is simply too small.

According to the well-established mechanism of steric stabilization, colloidal stability is achieved by creating a relatively thick dense surface layer of polymer chains.[2,30,53] In a good solvent for the stabilizer, interpenetration of such chains is unfavorable on both entropic and enthalpic grounds. This leads to a strong interparticle repulsive term that offsets the ever-present van der Waals attractive forces and ensures long-term colloidal stability. In principle, the stabilizer chains can be either chemically grafted[4,21,24] or merely physically adsorbed on the surface of the colloidal particles.[16−18] A third scenario arises for amphiphilic diblock copolymer nanoparticles, such as those prepared by polymerization-induced self-assembly (PISA) using techniques such as reversible addition−fragmentation chain transfer (RAFT) dispersion or emulsion polymerization.[20,54−70] In such cases the solvophilic block comprises the stabilizer chains, while the solvophobic block forms the particle core.

In the present work, we have exploited RAFT aqueous emulsion polymerization to prepare a series of near-monodisperse sterically stabilized diblock copolymer nanoparticles via PISA. The hydrophilic stabilizer block was chosen to be a well-known non-ionic water-soluble polymer, namely poly(glycerol monomethacrylate) [PGMA], while poly(2,2,2-trifluoroethyl methacrylate) [PTFEMA] was selected as the hydrophobic core-forming block, mainly because of its relatively high solid-state density (1.47 g cm^{-3}, see Figure 1). This model system was designed to enable the determination of the effective particle density ($\rho_{particle}$) and stabilizer shell thickness (T_{shell}) for sterically stabilized diblock copolymer nanoparticles. Initially, the nanoparticle size and morphology was assessed using transmission electron microscopy (TEM) and dynamic light scattering (DLS). SAXS was then utilized to determine the volume-average diameter, aggregation number (N_{agg}), and T_{shell} for selected nanoparticles. The latter data were then used to calculate an effective particle density ($\rho_{particle}$), which enabled high resolution particle size analysis for this model system via disk centrifuge photosedimentometry (DCP). Finally, it is demonstrated that DCP size distributions can be corrected for the superimposed density distribution that is an intrinsic feature of such core−shell nanoparticles.
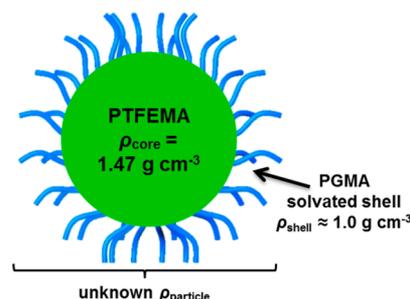

Figure 1. Schematic representation of a sterically stabilized PGMA$_x$−PTFEMA$_y$ diblock copolymer nanoparticle. The effective particle density ($\rho_{particle}$) in aqueous solution will depend on the radius and density of the PTFEMA core (ρ_{core}) and the thickness (T_{shell}) and density of the solvated stabilizer shell (ρ_{shell}).

■ EXPERIMENTAL SECTION

Materials. Glycerol monomethacrylate (GMA) was donated by GEO Specialty Chemicals (Hythe, UK) and used without further purification. 2,2,2-Trifluoroethyl methacrylate (TFEMA) and 4,4′-azobis(4-cyanopentanoic acid) (ACVA; 99%) were purchased from Sigma-Aldrich UK and were used as received. 2-Cyano-2-propyl dithiobenzoate (CPDB) was purchased from STREM Chemicals Ltd. (Cambridge, UK) and was used as received. d_6-Acetone and d_4-methanol were purchased from Goss Scientific Instruments Ltd. (Cheshire, UK). All other solvents were purchased from Fisher Scientific (Loughborough, UK) and used as received. Deionized water was used for all experiments.

Synthesis of PGMA$_x$ Macro-CTA via RAFT Solution Polymerization. A typical protocol for the synthesis of PGMA$_{63}$ is as follows. CPDB RAFT agent (1.650 g, 7.454 mmol), GMA (78.144 g, 488 mmol), and ACVA (0.379 g, 1.352 mmol; CPDB/ACVA molar ratio = 5.0) were weighed into a 500 mL round-bottom flask and degassed with nitrogen for 15 min. Ethanol (148 mL) was deoxygenated separately with nitrogen for 30 min prior to addition to the other reagents. The reaction solution was stirred and degassed in an ice bath for a further 30 min before placing in an oil bath at 70 °C. The polymerization was allowed to proceed for 150 min (GMA monomer conversion = 68% as judged by ^{1}H NMR). The crude homopolymer was collected by precipitation into a 10-fold excess of dichloromethane from methanol. This cleanup protocol was repeated twice to afford a pure PGMA macro-CTA (53.14 g, <1% residual monomer). The mean degree of polymerization (DP) was calculated to be 63 as judged by ^{1}H NMR. DMF GPC analysis indicated an M_n of 15 000 g mol^{-1} and an M_w/M_n of 1.19 (vs a series of near-monodisperse poly(methyl methacrylate) (PMMA) calibration standards). Other PGMA macro-CTAs with differing mean degrees of polymerization (28, 43, and 98) were prepared using a similar protocol simply by varying the monomer/CPDB molar ratio.

RAFT Aqueous Emulsion Polymerization of PGMA$_x$−PTFEMA$_y$. A typical protocol for the synthesis of PGMA$_{63}$−PTFEMA$_{400}$ diblock copolymer nanoparticles was as follows: PGMA$_{63}$ macro-CTA (0.140 g), ACVA (0.600 mg, 2.14 μmol; macro-CTA/ACVA molar ratio = 3.0), and water (4.58 g, 10% w/w) were weighed into a 14 mL sample vial, sealed with a rubber septum, and degassed with nitrogen for 30 min. TFEMA [3.20 mL, 22.6 mmol, target degree of polymerization (DP) = 400], which had been deoxygenated separately with nitrogen for 15 min, was then added to the solution under nitrogen and immersed in an oil bath set at 70 °C. The reaction solution was stirred for 20 h to ensure complete TFEMA monomer conversion, and the polymerization was quenched by exposure to air. ^{19}F NMR spectroscopy analysis of the copolymer dissolved in d_6-acetone indicated less than 1% residual TFEMA monomer. Four series of PGMA$_x$−PTFEMA$_y$ diblock copolymer nanoparticle dispersions were prepared by utilizing the PGMA$_x$ macro-CTAs described above and varying the degree of polymerization of the PTFEMA block (y) from 100 to 1400.
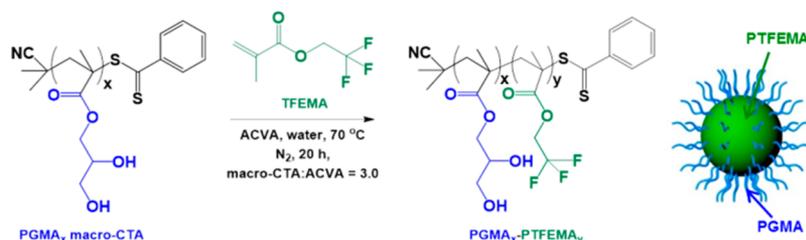
Figure 2. PISA synthesis of PGMA$_x$−PTFEMA$_y$ diblock copolymers via RAFT aqueous emulsion polymerization of TFEMA using a PGMA$_x$ macro-CTA at 70 °C to produce sterically stabilized spherical nanoparticles at 20% w/w solids.

^{1}H NMR Spectroscopy. All ^{1}H NMR spectra were recorded at 400 MHz in d_6-acetone or d_4-methanol using a Bruker Avance-400 spectrometer with 64 scans averaged per spectrum.

^{19}F NMR Spectroscopy. All ^{19}F NMR spectra were recorded at 377 MHz in d_6-acetone using either a Bruker Avance-400 spectrometer or Bruker Avance-500 spectrometer with 128 scans averaged per spectrum.

Gel Permeation Chromatography (GPC). The molecular weights and polydispersities of the PGMA macro-CTAs and selected PGMA$_x$−PTFEMA$_y$ diblock copolymers were determined by DMF GPC operating at 60 °C. The setup comprised two Polymer Laboratories PL gel 5 μm Mixed C columns connected in series to a Varian 390 LC multidetector suite (refractive index and ultraviolet detector) and a Varian 290 LC pump injection module. The GPC eluent was HPLC-grade DMF containing 10 mmol of LiBr with a flow rate of 1.0 mL min^{-1}. DMSO was used as a flow rate marker, and six near-monodisperse PMMA standards (M_p = 625−489 000 g mol^{-1}) were used for calibration. Chromatograms were analyzed using Varian Cirrus GPC software (version 3.3).

Helium Pycnometry. The solid-state density of PTFEMA homopolymer was determined using a Micromeritics AccuPyc 1330 helium pycnometer operating at 20 °C.

Transmission Electron Microscopy (TEM). Copper/palladium TEM grids (Agar Scientific, UK) were coated in-house with a thin film of amorphous carbon. The grids were then subjected to a glow discharge for 30 s to create a hydrophilic surface. Each aqueous diblock copolymer dispersion (0.20% w/w, 10.0 μL) was adsorbed onto a freshly treated grid for 1 min and then blotted with filter paper to remove excess solution. To stain the deposited nanoparticles, uranyl formate (9.0 μL of a 0.75% w/w aqueous solution) was placed on the sample-loaded grid for 20 s and then carefully blotted to remove excess stain. The grids were then dried using a vacuum hose. Imaging was performed using a Philips CM100 instrument operating at 100 kV and equipped with a Gatan 1 k CCD camera.

Dynamic Light Scattering (DLS). Hydrodynamic particle diameters were obtained using a Malvern Zetasizer NanoZS instrument, equipped with a 4 mW He−Ne solid-state laser operating at 633 nm. Backscattered light was detected at 173°, and the mean particle diameter was calculated from the quadratic fitting of the correlation function using the Stokes−Einstein equation. Highly dilute aqueous dispersions were analyzed using disposable plastic cuvettes after equilibrating at 25 °C for 30 s; all measurements were performed in triplicate and averaged values reported.

Small-Angle X-ray Scattering (SAXS). Small-angle X-ray scattering patterns were acquired at a synchrotron source (Diamond Light Source, station I22, Didcot, UK) using monochromatic X-ray radiation and a 2D Pilatus 2M pixel detector (wavelength, λ = 1.0 Å, camera length = 10 m, which gives a q range from 0.002 to 0.2 Å^{-1}, where $q = 4\pi \sin \theta/\lambda$ is the length of the scattering vector and θ is half of the scattering angle). A polycarbonate capillary cell of 2 mm diameter was used as a sample holder for dilute (1.0% w/w) aqueous dispersions of the PGMA$_x$−PTFEMA$_y$ nanoparticles. 2D scattering data were reduced to 1D patterns using Dawn software developed at the Diamond Light Source. Further data processing (background subtraction and calibration to absolute intensity) and analysis were performed using Irena SAS macros for Igor Pro.[71]

SAXS patterns were also acquired for the four PGMA$_x$ macro-CTAs and selected nanoparticles using a Bruker AXS Nanostar instrument equipped with a 2D HiSTAR multiwired gas detector, modified with a Xenocs microfocus Genix 3D X-ray source (Cu Kα radiation), a collimator composed of motorized scatterless slits (Xenocs, France), and camera length of 1.46 m. SAXS patterns were recorded over a scattering vector range of 0.008 Å^{-1} < q < 0.16 Å^{-1}, using thin-walled 2 mm glass capillaries. Scattering data were reduced using Irena Nika macros for Igor Pro and analyzed using Irena SAS macros.[71]

Disk Centrifuge Photosedimentometry (DCP). A CPS Instruments model DC24000 disk centrifuge photosedimentometer was used to obtain weight-average particle size distributions. This instrument employed a 405 nm diode sensor for particle detection via turbidimetry (i.e., change in absorbance) near the disk periphery at the maximum centrifugation rate of 24 000 rpm. After reaching this speed, a density gradient was generated *in situ* by filling the empty disc with an aqueous sucrose spin fluid (14.4 mL). Measurements were conducted using a 2−8% w/w aqueous sucrose gradient as the spin fluid, with n-dodecane (0.50 mL) being added to prevent water evaporation and hence extend the gradient lifetime. The instrument was calibrated by injecting 100 μL of either 239 or 263 nm near-monodisperse poly(vinyl chloride) (PVC) latex particles (CPS Instruments, Seagate Lane, Stuart, FL), followed by injection of 100 μL of PGMA$_x$−PTFEMA$_y$ diblock copolymer nanoparticles in the form of a 1−5% w/w aqueous dispersion.

■ RESULTS AND DISCUSSION

Copolymer Synthesis. Four PGMA$_x$ macro-CTAs were synthesized via RAFT solution polymerization in ethanol at 70 °C. These homopolymers had mean degrees of polymerization of 28, 43, 63, and 98 with DMF GPC analysis indicating narrow polydispersities (M_w/M_n < 1.15) in each case. Chain extension of these PGMA$_x$ macro-CTAs using the water-insoluble TFEMA monomer (aqueous solubility = 0.40 g dm^{-3} at 20 °C) via RAFT aqueous emulsion polymerization yielded four series of PGMA$_x$−PTFEMA$_y$ (denoted as G$_x$-F$_y$ for brevity) diblock copolymers (Figure 2). As expected, *in situ* self-assembly led to the formation of well-defined spherical nanoparticles with PTFEMA cores and PGMA stabilizer shells. A series of diblock copolymers were prepared by varying the target DP of the core-forming PTFEMA block. In principle, systematic variation of the mean DP of the PTFEMA block enables the nanoparticle size to be tuned.[64] Similarly, varying the DP of the PGMA stabilizer block allows the stabilizer layer thickness to be adjusted, as desired.

Each polymerization proceeded to high conversion, as judged by both ^{1}H and ^{19}F NMR spectroscopy (see Table 1). The ^{19}F NMR spectrum for TFEMA monomer comprises a sharp triplet at −74.5 ppm; the corresponding PTFEMA exhibits a relatively broad signal at −73.9 ppm (see spectra A and C in Supporting Information Figure S1). Comparison of these two integrated signals provides a sensitive method for calculating the monomer conversion, since ^{19}F is 100% abundant. Moreover,

Table 1. Summary of TFEMA Conversion and Mean Intensity-Average (DLS) and Number-Average (TEM) Diameters Obtained for PGMA$_x$–PTFEMA$_y$ Diblock Copolymer Nanoparticles Prepared via RAFT Aqueous Emulsion Polymerization

targeted sample composition[a]	conversion (%)		particle diameter (nm)	
	^{1}H NMR	^{19}F NMR	DLS	TEM[b]
G$_{28}$-F$_{100}$	>99	>99	42 ± 14	33 ± 3
G$_{28}$-F$_{200}$	>99	>99	77 ± 22	63 ± 7
G$_{28}$-F$_{300}$	>99	>99	104 ± 20	81 ± 8
G$_{28}$-F$_{400}$	99	99	136 ± 20	113 ± 14
G$_{28}$-F$_{500}$	98	99	169 ± 36	146 ± 18
G$_{43}$-F$_{400}$	99	99	87 ± 18	61 ± 7
G$_{43}$-F$_{600}$	99	99	130 ± 21	105 ± 9
G$_{43}$-F$_{800}$	99	>99	189 ± 22	144 ± 12
G$_{43}$-F$_{1000}$	99	>99	246 ± 9	174 ± 18
G$_{63}$-F$_{123}$	>99	>99	34 ± 16	23 ± 3
G$_{63}$-F$_{184}$	>99	>99	46 ± 13	32 ± 4
G$_{63}$-F$_{246}$	>99	>99	53 ± 13	35 ± 5
G$_{63}$-F$_{369}$	>99	99	71 ± 20	42 ± 6
G$_{63}$-F$_{400}$	99	99	73 ± 19	63 ± 7
G$_{63}$-F$_{430}$	99	99	84 ± 26	56 ± 8
G$_{63}$-F$_{492}$	98	>99	91 ± 13	62 ± 10
G$_{63}$-F$_{615}$	99	99	110 ± 13	89 ± 9
G$_{63}$-F$_{737}$	97	98	127 ± 16	88 ± 12
G$_{63}$-F$_{983}$	99	99	156 ± 30	104 ± 11
G$_{63}$-F$_{1106}$	99	99	170 ± 25	140 ± 13
G$_{63}$-F$_{1230}$	91	92	188 ± 20	164 ± 17
G$_{98}$-F$_{400}$	99	99	61 ± 18	49 ± 8
G$_{98}$-F$_{600}$	99	99	88 ± 18	58 ± 10
G$_{98}$-F$_{800}$	99	99	106 ± 14	79 ± 10
G$_{98}$-F$_{1000}$	>99	>99	132 ± 22	98 ± 17
G$_{98}$-F$_{1400}$	92	94	161 ± 24	129 ± 19

[a]This was assumed to be equal to the actual composition on account of the high monomer conversions, with the exception of G$_{63}$-F$_{737}$, G$_{63}$-F$_{1230}$, and G$_{98}$-F$_{1400}$. The actual diblock compositions of these samples were estimated to be G$_{63}$-F$_{719}$, G$_{63}$-F$_{1125}$, and G$_{98}$-F$_{1302}$, respectively. [b]At least 100 particles were counted in each case.

unlike ^{1}H NMR spectra, ^{19}F NMR spectra do not suffer from overlapping signals arising from other species (see spectrum B in Figure S1).

For GPC analysis of diblock copolymers using a refractive index (RI) detector, there is an implicit assumption that the two blocks have comparable refractive indices. However, in this case the RI of the PTFEMA block is 1.42,[72] which is close to that of the DMF eluent (1.43)[73] and significantly lower than that of most non-fluorinated methacrylic polymers (RI = 1.49–1.59). Thus, the RI detector necessarily underestimates the relative signal intensity due to the semi-fluorinated block, which in turn exaggerates the apparent contamination of the diblock copolymer by the macro-CTA.[74] Indeed, DMF GPC analysis of the dissolved diblock copolymer chains using an RI detector indicated a prominent low molecular weight shoulder, which would normally suggest poor blocking efficiency for the PGMA$_x$ (see graph A in Figure S2). However, this shoulder was substantially suppressed when using a UV GPC detector at 305 nm (which corresponds to the λ_{max} for the thiocarbonyl chain-end chromophore). Thus, in reality, relatively high blocking efficiencies were achieved during the synthesis of

these diblock copolymer nanoparticles via RAFT aqueous emulsion polymerization (see graph B in Figure S2).

Initial Particle Characterization. In all cases the diblock copolymer nanoparticle dispersions prepared at 20% w/w solids were free-flowing, which suggested that spherical particles were obtained, rather than higher order morphologies such as worms.[68,75] DLS studies were conducted on dilute dispersions of the G$_x$-F$_y$ nanoparticles (summarized in Table 1). The intensity-average particle diameter increased monotonically as the PTFEMA target DP was increased (see Figure 3).
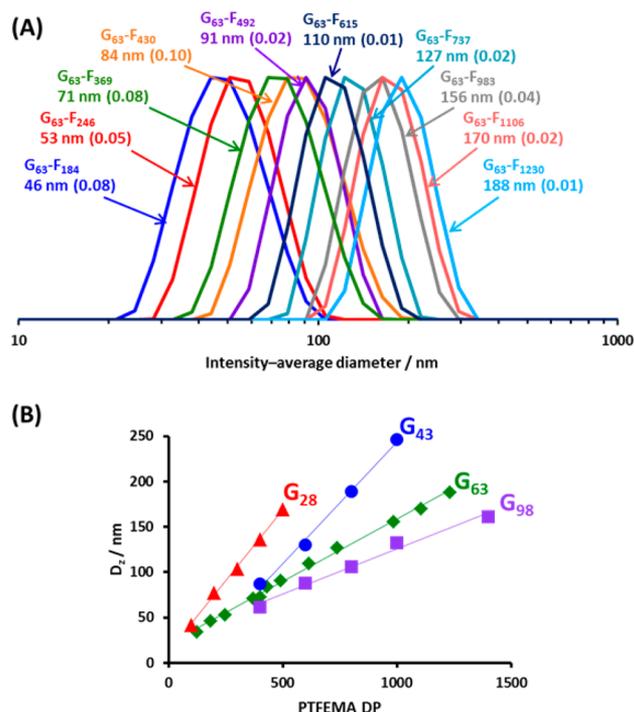

Figure 3. (a) DLS intensity-based size distributions obtained for G$_{63}$-F$_y$ particles prepared at 20% w/w solids via RAFT aqueous emulsion polymerization of TFEMA at 70 °C. (b) Linear correlation between the DLS intensity-average particle diameter and the mean degree of polymerization (DP) of the PTFEMA core-forming block.

DLS polydispersity indices were relatively low (typically <0.10) in each case, indicating relatively narrow size distributions for G$_x$-F$_y$ nanoparticles prepared using all four PGMA$_x$ macro-CTAs. However, using longer macro-CTAs invariably produced smaller nanoparticles when targeting a given PTFEMA DP (see Figure 3B).

TEM studies confirmed that only spherical morphologies were obtained, regardless of the G$_x$-F$_y$ diblock composition that was targeted (see Figure 4 and Figure S3). This kinetically trapped morphology has also been reported for the synthesis of many other diblock copolymer nanoparticles via RAFT aqueous emulsion polymerization.[54,58,64,76] However, it is noted that amphiphilic PTFEMA-based diblock copolymers can form the full range of copolymer morphologies (i.e., spheres, worms, and vesicles) when prepared via RAFT *dispersion* polymerization conducted in *ethanol*.[74] Given that such a striking difference is observed for the same core-forming block for syntheses performed at the same polymerization temperature (70 °C), it seems likely that insufficient *solvation* of the growing core-forming chains prevents reorganization to so-called higher order morphologies during RAFT aqueous emulsion polymer-
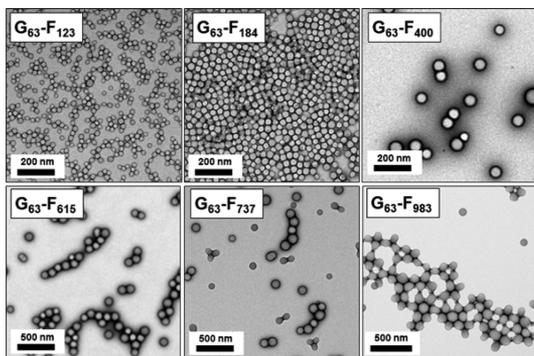
Figure 4. Representative TEM images recorded for G_{63}-F_y diblock copolymer nanoparticles prepared by RAFT aqueous emulsion polymerization of TFEMA using a PGMA$_{63}$ macro-CTA at 20% w/w solids. A well-defined spherical morphology is observed in each case, with larger particles being obtained when targeting longer core-forming PTFEMA blocks (for a given PGMA block DP).

ization. Thus, our hypothesis is that the relatively low solubility of TFEMA monomer in water (as opposed to ethanol) leads to reduced solvation of the growing PTFEMA chains during PISA.

Taking into account the effect of polydispersity and the steric stabilizer layer thickness, the mean number-average particle diameters calculated from TEM studies were in fairly good agreement with DLS studies (see Table 1). Again, it was observed that, for a given PGMA DP, increasing the target PTFEMA DP produced progressively larger nanoparticles.

Core–Shell Particle Density. The density of core–shell particles, $\rho_{particle}$, can be described by the relationship

$$\rho_{particle} = \frac{\rho_{core} V_{core} + \rho_{shell} V_{shell}}{V_{particle}}$$

$$= \frac{\rho_{core} R_{core}^3 + \rho_{shell}[(R_{core} + T_{shell})^3 - R_{core}^3]}{(R_{core} + T_{shell})^3} \quad (1)$$

where ρ_{core} and V_{core} represent the density and volume of the core component, ρ_{shell} and V_{shell} represent the density and volume of the shell component, and $V_{particle}$ is the overall volume of the particle.

For sterically stabilized nanoparticles comprising a solvent-free PTFEMA core with $\rho_{core} = 1.47$ g cm^{-3} and a highly hydrated PGMA shell such that $\rho_{shell} \approx 1.00$ g cm^{-3}, eq 1 was used to calculate $\rho_{particle}$ as a function of the core radius (R_{core}) for various (assumed) shell thicknesses T_{shell} (see Figure 5).
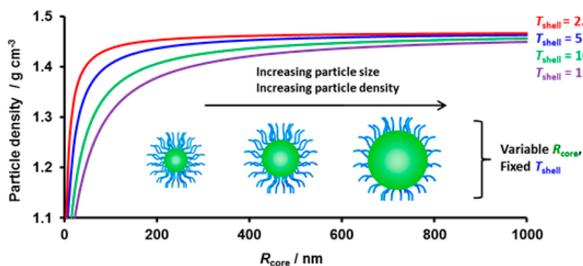

Figure 5. Relationship between particle density ($\rho_{particle}$) and core radius (R_{core}) for G_x-F_y diblock copolymer nanoparticles of constant shell thickness (T_{shell}). The particle density was calculated assuming a PGMA stabilizer shell density of 1.00 g cm^{-3}, a PTFEMA core density of 1.47 g cm^{-3}, and a fixed PGMA shell thickness of 2.5, 5.0, 10, or 15 nm.

For $R_{core} \leq 100$ nm with a T_{shell} of between 2.5 and 15 nm, $\rho_{particle}$ is strongly dependent on R_{core}. However, for particles with a sufficiently large R_{core} with respect to T_{shell}, there is a plateau region for which $\rho_{particle}$ is no longer strongly dependent on R_{core}. It is also evident that the shell thickness has a strong influence on the particle density, especially when the core radius is relatively small ($R_{core} \leq 100$ nm). Finally, it is noted that RAFT aqueous emulsion polymerization provides convenient access to a wide range of well-defined nanoparticles for which $R_{core} \leq 110$ nm.

In order to calculate the actual range of effective particle densities for the G_x-F_y particles discussed herein, it is important to obtain experimental values of V_{core} and V_{shell} (and hence R_{core} and T_{shell}). In principle, this information can be obtained by determining the difference between the intensity-average hydrodynamic diameter reported by DLS for the hydrated nanoparticles in solution and the number-average diameter calculated from TEM analysis of the dried nanoparticles. However, in practice, this approach is unsatisfactory because DLS and TEM are biased toward different moments of the particle size distribution. Thus, SAXS, which is a much more statistically robust and rigorous technique, was used in order to determine the required structural information for these G_x-F_y particles.

Small-Angle X-ray Scattering. SAXS patterns were recorded for 1.0% w/w dispersions of the G_x-F_y copolymer nanoparticles. Figure S4 shows the radially integrated patterns expressed as the scattering intensity vs the scattering vector, q. In all cases, the gradient of the scattering patterns at low q (Guinier region) is approximately zero, supporting the spherical particle morphology observed by TEM studies (Figure 4). The semi-fluorinated PTFEMA core-forming block has a relatively high scattering length density ($\xi_{PTFEMA} = 12.76 \times 10^{10}$ cm^{-2}) compared to the highly hydrated PGMA shell ($\xi_{PGMA} = 11.94 \times 10^{10}$ cm^{-2}, $\xi_{water} = 9.42 \times 10^{10}$ cm^{-2}), so the X-ray scattering is dominated by the former component. The position of the first minimum in each pattern associated with the particle form factor is inversely proportional to particle radius; as expected, this feature shifts to lower q for larger particles (higher PTFEMA DPs). It is also noteworthy that in most cases three or four minima are observed. This indicates relatively narrow particle size distributions and suggests that the q range chosen is appropriate for characterizing these nanoparticles.

The scattering intensity resulting from the PGMA chain/water shells at high q is relatively weak in comparison to the PTFEMA cores. Furthermore, when fitting scattering data it is important to minimize the number of adjustable parameters in any given model.[77] Thus, the radius of gyration (R_g) for each of the four PGMA$_x$ homopolymers dissolved in aqueous solution was determined by SAXS before modeling the scattering patterns obtained for the G_x-F_y diblock copolymer nanoparticles.

To determine R_g experimentally, a 1.0% w/w aqueous solutions of each PGMA$_x$ homopolymer was analyzed using a Gaussian coil model (see Supporting Information section C).[78] The two fitting parameters used for this model are R_g and ν; the latter corresponds to the excluded volume fraction governed by the polymer–solvent interaction. Scattering patterns and models are shown in Figure 6. As expected, the normalized scattering intensity depends on the chain length, with the longest PGMA$_x$ ($x = 98$) producing the greatest normalized scattering intensity. In each case ν was fixed at 0.50, which corresponds to theta solvent conditions. Prediction of the
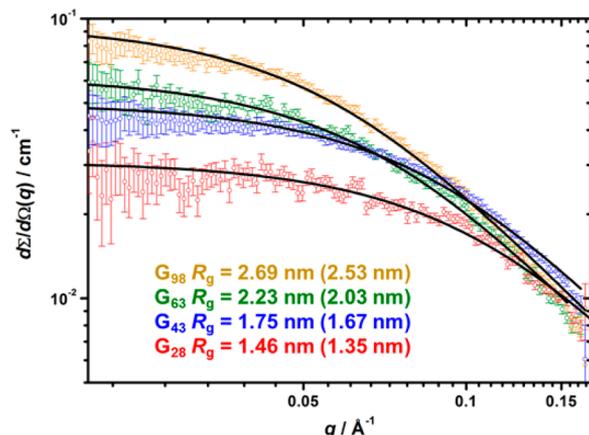
Figure 6. Small-angle X-ray scattering patterns recorded for 1.0% w/w aqueous solutions of PGMA$_x$ homopolymer chains. Solid lines represent fits to the data using a Gaussian coil model (see Table S1 and section C in the Supporting Information). The R_g values obtained from this model using ν = 0.5 are given, and the numbers in parentheses refer to the theoretical values.

Figure 7. Selected small-angle X-ray scattering patterns (colored circles) recorded for 1.0% w/w aqueous solutions of G$_x$-F$_y$ nanoparticles at 20 °C. Solid black lines represent fits to the data using a spherical micelle model.[78]

scattering intensity at low q is summarized in section C of the Supporting Information. Calculated values correlate well with the experimental data and support highly hydrated polymer chains in dilute aqueous solution (see Table S1). R_g values of 1.46, 1.75, 2.23, and 2.69 nm were obtained for the four PGMA$_x$ homopolymers (where x equals 28, 43, 63, or 98, respectively). Theoretical values of R_g were also estimated from total chain contour lengths and Kuhn length. The contour length, L_{PGMA}, for the PGMA$_x$ block, is approximately given by L_{PGMA} = number of GMA units × 0.255 nm, where 0.255 nm is the projected contour length per monomer repeat unit (as defined by two carbon bonds in an *all-trans* conformation). A Kuhn length of 1.53 nm corresponds to the literature value for poly(methyl methacrylate).[79] Consequently, it follows that R_g = $(L_{PGMA} \times 1.53/6)^{1/2}$.[79] This approach gave theoretical R_g values of 1.35, 1.67, 2.03, and 2.53 nm for the four PGMA homopolymers comprising 28, 43, 63, and 98 GMA monomer units, respectively. These calculated values are in relatively good agreement with the experimental values (see Table S1). However, the experimentally determined R_g values are preferred as no assumptions regarding contour or Kuhn lengths are required.

In order to model the scattering data obtained for G$_x$-F$_y$ nanoparticles, the PGMA shell thickness was taken to be equal to 2R_g, and the former parameter was assumed to remain constant for a given PGMA DP, regardless of the PTFEMA DP. Furthermore, preliminary modeling indicated a mean value for the solvation of the PTFEMA core (x_{sol}) of approximately 0.05, or just 5% solvent within the PTFEMA cores. This seems reasonable given the highly hydrophobic character of this block (its solvent interaction parameter, χ_{H_2O}, is approximately 7.30).[80] Using the aforementioned R_g and x_{sol} values and a least-squares fit, a spherical micelle model[78] was used to fit SAXS patterns obtained for a subset of diblock copolymer nanoparticles comprising a variable PGMA stabilizer DP and a core-forming PTFEMA DP of up to 400, for which R_{core} ≤ 37 nm (Figure 7). A detailed description of the model and fitting parameters used to analyze these SAXS patterns is given in the Supporting Information (see section C and Table S2). It should
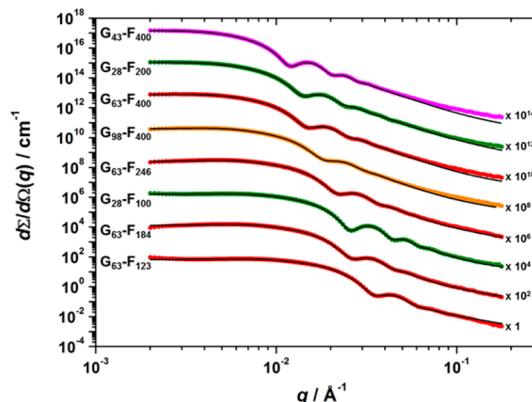
be noted that an appropriate structure factor had to be included in the model in order to obtain reasonably good fits to the data.

For relatively small nanoparticles (PTFEMA DP ≤ 400, or R_{core} ≤ 37 nm), the spherical micelle model produced good data fits over the whole q range (Figure 7). However, for larger nanoparticles, a systematic deviation between experimental scattering patterns, and the corresponding data fits were observed at high q (see Figure S4). Despite this technical problem, the SAXS results obtained for R_{core} were fully consistent with DLS data shown in Table 1. Inspecting Figure 5, it is clear that the greatest change in effective particle density occurs for small nanoparticles (R_{core} ≤ 100 nm), and it is emphasized that the SAXS data fits are robust in this regime. Notwithstanding the less satisfactory data fits obtained for the larger nanoparticles, SAXS enables R_{core} to be determined with reasonable accuracy (see following section).

For a fixed PTFEMA DP, both the nanoparticle core radius and the overall nanoparticle diameter increase when using shorter PGMA stabilizer blocks. This can be explained by considering the number of copolymer chains per nanoparticle, N_{agg}, which is calculated using the equation

$$N_{agg} = (1 - x_{sol}) \times \frac{4}{3}\pi \times \frac{R_{core}^3}{V_{chain}} \quad (2)$$

where V_{chain} is the volume occupied by PTFEMA in a single copolymer chain. As the PGMA DP increases for the G$_x$-F$_{400}$ nanoparticles, N_{agg} is reduced from approximately 2600 to 600 (see gray box in Figure 8). This is because longer stabilizer blocks occupy a larger interfacial area between the nanoparticle core and shell.[81] Moreover, there is a reduction in the R_{core}/L_{PTFEMA} ratio, which provides a measure of the degree of chain coiling within the core (here L_{PTFEMA} is estimated from the *trans* C−C bond length assuming a fully stretched chain). R_{core}/L_{PTFEMA} is reduced from 0.36 for nanoparticles stabilized using G$_{43}$ to 0.29 and 0.23 for G$_{63}$ and G$_{98}$, respectively. This suggests that for longer PGMA stabilizer chains, which produce nanoparticles with lower aggregation numbers, the hydrophobic PTFEMA chains are more compact within the (smaller) nanoparticle cores.

For a given PGMA DP, N_{agg} increases as the DP of PTFEMA becomes larger (Figure 7). This observation correlates well with the monotonic increase in intensity-average diameter indicated by DLS studies; hence, particle growth is a
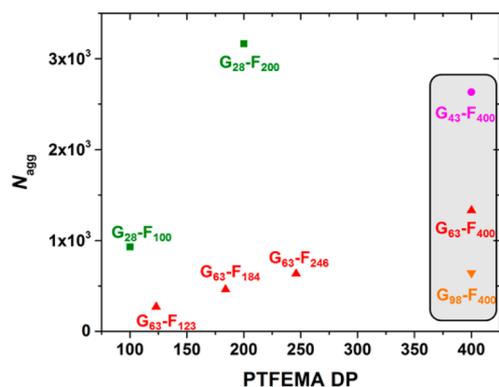
Figure 8. Relationship between aggregation number (N_{agg}) and core-forming block DP for selected G_x-F_y nanoparticles prepared using PGMA$_{28}$ (■), PGMA$_{43}$ (●), PGMA$_{63}$ (▲), and PGMA$_{98}$ (▼) macro-CTAs.

consequence of both the greater PTFEMA chain length and a larger number of copolymer chains per particle.

Calculation and Implications of Effective Particle Density. For the data sets shown in Figure S4, the SAXS patterns between $q = 0.005$ Å^{-1} and $q = 0.05$ Å^{-1} were used to calculate the mean core radius, R_{core}, for each nanoparticle dispersion using the spherical micelle model. Combining this information with the R_g data obtained by SAXS analysis of the corresponding PGMA stabilizer chains in aqueous solution enabled the effective particle density, $\rho_{particle}$, to be determined using eq 1 (see Figure 9).
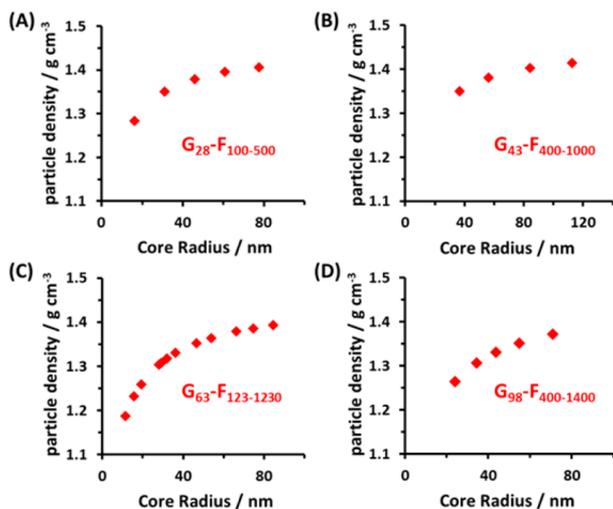

Figure 9. Effective particle densities ($\rho_{particle}$) calculated for G_x-F_y nanoparticles using structural parameters derived from SAXS analysis. The weak solvation of the core-forming PTFEMA block indicated by SAXS was taken into account (effective $\rho_{core} = 1.45$ g cm^{-3}) and ρ_{shell} for the highly hydrated shell was taken to be that of water (1.00 g cm^{-3}).

In this analysis, ρ_{core} was taken to be 1.45 g cm^{-3} (i.e., 5% solvent is assumed within the nanoparticle cores, as indicated from SAXS data fits) and ρ_{shell} was assumed to be 1.00 g cm^{-3} (we estimate that the volume fraction of the PGMA chains within the stabilizer shell does not exceed 0.01). Thus, it is clear that the effective particle density, $\rho_{particle}$, of these sterically stabilized G_x-F_y nanoparticles depends markedly on the precise x and y values and varies from 1.19 g cm^{-3} (for G_{63}-F_{123}) up to

approximately 1.41 g cm^{-3} as the core radius approaches 80 nm.

It is also noteworthy that over the same core size range the G_{28} series ($T_{shell} = 2.92$ nm) have effective particle densities which are consistently higher than particles stabilized by G_{98} ($T_{shell} = 5.38$ nm). Such drastic changes in effective density over a relatively narrow range of particle compositions and diameters can have important implications when conducting particle size analyses using certain commercial instruments.

For example, DCP is a widely used, high-resolution particle sizing technique that has been used to characterize a wide range of colloidal particles including copolymer latexes,[82−87] viruses,[88−91] colloidal nanocomposites,[50,92−100] protein-coated particles,[101] and various inorganic nanoparticles.[35,102−109] DCP is based on the principle of centrifugal sedimentation: particles are radially fractionated within a rotating disk according to their size and relative density; i.e., for particles with uniform density, large particles sediment more quickly than small particles. For calculating accurate particle size distributions using DCP, the effective particle density is an essential input parameter.

Accordingly, weight-average particle size distributions were determined by DCP for the G_x-F_y nanoparticles discussed herein (see Figure S5). The effective particle densities used to determine these particle size distributions were calculated from SAXS analysis (see Figure 9). In most cases, these size distributions are relatively narrow and the trend in mean-particle diameter agrees well with the DLS, TEM, and SAXS diameters. In addition, there is no evidence of flocculation in these particle size distributions; Balmer and co-workers have recently shown that DCP is very sensitive to such incipient aggregation.[95]

In order to illustrate the importance of using an accurate particle density for DCP analysis, Figure 10 shows an example of a particle size distribution determined for G_{63}-F_{184} nanoparticles using the solid-state density of PTFEMA (1.47 g cm^{-3}, blue line). When compared to the particle size
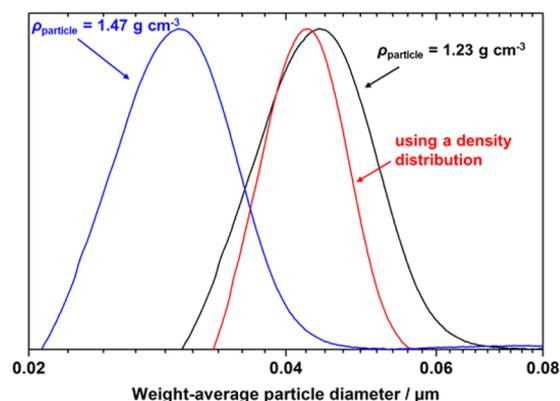

Figure 10. Weight-average particle size distributions determined by disk centrifuge photosedimentometry (DCP) for G_{63}-F_{184} nanoparticles. The blue curve shows the *erroneous* size distribution obtained for G_{63}-F_{184} nanoparticles when an upper limit density of 1.47 g cm^{-3} (which corresponds to the solid-state density of dry PTFEMA homopolymer) is used for DCP analysis. The black curve shows the *corrected* particle size distribution obtained when a *single* effective particle density is used (1.23 g cm^{-3}). The red curve is the *true* particle size distribution recalculated to account for the *density distribution* that is superimposed on the particle size distribution (see Table 2). However, the latter refinement becomes negligible for relatively large G_x-F_y nanoparticles (see Figure S6).

distribution determined using a corrected effective particle density (black line), it is clear that the former erroneous size distribution substantially underestimates the mean diameter of the G_{63}-F_{184} nanoparticles.

At this point it is perhaps worth noting that analytical centrifugation techniques have previously been employed to determine effective particle densities for various nanoparticles by applying Stokes' law to determine particle velocities in media of differing densities.[91,107] However, in the present case this approach would not account for the change in density of the stabilizer shell, since this largely comprises the spin fluid (or continuous phase). As a consequence, $\rho_{particle}$ is not constant and depends on the spin fluid density. Thus, we find it more appropriate to use the calculated effective densities based on SAXS analysis rather than relying on the former techniques.

An inherent assumption made during DCP analysis is that all particles are of equal density. In reality, the stabilizer shell thickness is essentially constant, but there is some variation in the nanoparticle core diameter, as confirmed by the TEM images shown in Figure 4. Consequently, larger particles possess slightly higher densities and so a density distribution is imposed on the particle size distribution. Interestingly, this density distribution for sterically stabilized nanoparticles (comprising low density shells and high density cores) is *complementary* to that previously reported by Fielding et al. for polystyrene/silica nanocomposite particles (i.e., high density shells and low density cores).[50] In this earlier study, it was shown that a mathematical method could be employed to correct for this density distribution, which enabled the raw DCP data to be reanalyzed in order to calculate true particle size distributions. Furthermore, these recalculated particle size distributions were both broader than those reported using a single density and also more consistent with particle size distributions reported using other sizing techniques.

Accordingly, a similar approach to that described previously[50] was used herein to correct for the density distribution in the case of a core–shell particle morphology in which the high-density PTFEMA core is of variable diameter and the low-density PGMA stabilizer shell is of fixed thickness (see Supporting Information section D). Specifically, absorbance versus time raw data sets obtained from DCP measurements were analyzed assuming a "best guess" particle density (ρ) to calculate an apparent diameter at the time of detection (D_t). The resulting D_t versus time data sets were then reanalyzed using a model that relates D_t to the true particle diameter (D_p) according to the following equation:

$$\Delta_p (D_p/T_{shell})^2 = 4(\rho_{particle} - \rho_{fluid})(r+1)^2 = \Delta_0 (D_t/T_{shell})^2 \tag{3}$$

Here Δ_p is the difference between the density of the core–shell particle ($\rho_{particle}$) and that of the spin fluid (ρ_{fluid}), and the density difference, Δ_0, is $\rho - \rho_{fluid}$. For particles with a uniform shell thickness (T_{shell}) and a given core radius (R_{core}), $\rho_{particle}$ can be given by simplifying eq 1 as follows:

$$\rho_{particle} = \frac{\rho_{core} r^3 + \rho_{shell}[(r+1)^3 - r^3]}{(r+1)^3} \tag{4}$$

where ρ_{core} and ρ_{shell} are the densities of the core and shell, respectively, and r is the dimensionless variable

$$r = R_{core}/T_{shell} \tag{5}$$

Substituting eq 4 into eq 3 yields a cubic equation (see Supporting Information eq D5) that can be solved to give a physically realistic D_p value for every D_t calculated during the original DCP measurement. This model is actually less complex than that reported previously because it leads to a *cubic* equation, rather than the *quintic* equation derived earlier.[50] The additional complexity of the earlier model arises from the need to account for the particulate nature of the shell.[50] A FORTRAN77 program (see section E in the Supporting Information) was written in order to solve the cubic equation (eq D5) for its single real positive root and hence recalculate the true weight-average particle size distributions for a given set of G_x-F_y data obtained by DCP.

Figure 10 shows the DCP data for the G_{63}-F_{184} particles (for which SAXS indicates an R_{core} of 16 nm, see entry 1 in Table 2).

Table 2. Summary of Effective Particle Densities and Particle Diameters Determined by Both SAXS and DCP for PGMA$_{63}$–PTFEMA$_y$ Diblock Copolymer Nanoparticles Prepared via RAFT Aqueous Emulsion Polymerization[a]

		particle diameter (nm)		
diblock copolymer composition	effective particle density, $\rho_{particle}$ (g cm^{-3})	SAXS ($2R_{core}$ + $4R_g$)	DCP using $\rho_{particle}$	DCP using $\rho_{particle}$ distribution
G_{63}-F_{184}	1.23	41 ± 4	45 ± 6	43 ± 4
G_{63}-F_{430}	1.32	72 ± 8	72 ± 8	72 ± 7
G_{63}-F_{615}	1.35	101 ± 10	101 ± 12	101 ± 11
G_{63}-F_{1106}	1.39	157 ± 12	146 ± 16	147 ± 14

[a]The DCP particle diameters were determined using both a *single* effective particle density ($\rho_{particle}$) and also by superimposing an *effective density distribution* on the particle size distribution.

As discussed above, the DCP trace obtained when using a particle density of 1.47 g cm^{-3} (blue line) clearly undersizes these nanoparticles when compared to the corresponding TEM, DLS, and SAXS data. A more realistic particle size distribution is reported when using an appropriate effective particle density of 1.23 g cm^{-3} (black line). The red trace shows the particle size distribution obtained when the data has been recalculated to account for the superimposed density distribution. As expected, the recalculated distribution is *narrower* than that determined using a single-value effective particle density. However, this effect is only significant for smaller nanoparticles, where the volume fraction of the hydrated PGMA stabilizer layer is relatively high, leading to a more pronounced variation in the particle density (Figure 9). Figure S6 shows that as the nanoparticle mean diameter increases, the recalculation becomes less significant, and Table 2 summarizes the differences in the reported weight-average diameters along with SAXS data and particle densities for comparison (i.e., a subset of those shown in graph C of Figure S5). In principle, this correction will also be negligible for highly monodisperse particles, since there is minimal variation in the nanoparticle core volume in this case.

The above technical solution to the problem of a superimposed density distribution for core–shell particles comprising high-density cores and low-density shells has been formulated for a model system of sterically stabilized diblock copolymer nanoparticles. However, the approach is generic and hence is expected to be useful for various colloidal dispersions reported in the literature, including sterically stabilized gold

nanoparticles[108−111] and sterically stabilized magnetite sols,[112−116] both of which are used for biomedical applications.

CONCLUSIONS

Four series of PGMA$_x$−PTFEMA$_y$ diblock copolymers were prepared using RAFT aqueous emulsion polymerization. Very high conversions (typically >99%) were achieved, as judged by ^{19}F NMR spectroscopy analysis. These diblock copolymers exhibited narrow, unimodal molecular weight distributions as judged by UV GPC analysis. Self-assembly in solution is driven by the *in situ* growth of the highly hydrophobic PTFEMA block, yielding sterically stabilized spherical nanoparticles with relatively narrow size distributions, as confirmed by TEM studies. Judicious variation of the PGMA$_x$−PTFEMA$_y$ diblock composition allowed the mean nanoparticle diameter to be controlled over a relatively wide range, from ∼30 to ∼250 nm. For a fixed DP of the hydrophilic PGMA stabilizer, a monotonic increase in particle diameter was observed on increasing the DP of the core-forming PTFEMA block. On the other hand, a substantial reduction in particle diameter was observed for PGMA$_x$−PTFEMA$_{400}$ nanoparticles on increasing the PGMA stabilizer DP (or x). SAXS analysis indicated a corresponding smaller mean number of copolymer chains per spherical nanoparticle, N_{agg}.

The radius of gyration, R_g, of the PGMA$_x$ precursor chains in aqueous solution was calculated theoretically and also determined experimentally via SAXS. The latter value was subsequently used as a fixed parameter (along with x_{sol}) when modeling SAXS patterns recorded for PGMA$_x$−PTFEMA$_y$ diblock copolymer nanoparticles in aqueous solution. This approach enabled calculation of effective particle densities for these model sterically stabilized nanoparticles, which is an essential parameter for reliable particle size analysis via analytical centrifugation. As expected, a significant increase in effective particle density was observed as the mole fraction of the high-density PTFEMA core component was increased. This model system was designed to enable the determination of the effective particle density and stabilizer layer thickness for sterically stabilized diblock copolymer nanoparticles. SAXS was then utilized to determine the volume-average diameter, N_{agg}, and stabilizer shell thickness. These structural parameters were used to calculate an effective particle density, which enabled high resolution particle size analysis to be conducted for this model system via disk centrifuge photosedimentometry. Finally, the resulting particle size distributions were corrected for the superimposed density distribution that is an intrinsic feature of such core−shell nanoparticles. This led to narrower size distributions, and this correction is expected to be applicable to other colloidal dispersions reported in the literature.

ASSOCIATED CONTENT

Ⓢ Supporting Information

The Supporting Information is available free of charge on the ACS Publications website at DOI: 10.1021/acs.macromol.6b00987.

19F NMR spectra of TFEMA monomer and PTFEMA homopolymer; gel permeation chromatograms of PGMA$_{63}$ homopolymer and PGMA$_{63}$−PTFEMA$_y$ copolymers; TEM images of PGMA$_x$−PTFEMA$_y$ particles; small-angle X-ray scattering patterns, fitting parameters and model descriptions for PGMA$_x$ homopolymers and PGMA$_x$−PTFEMA$_y$ particles; particle size distributions

determined by disk centrifuge photosedimentometry; derivation of equation and FORTRAN77 program used to correct disk centrifuge data (PDF)

AUTHOR INFORMATION

Corresponding Authors
*E-mail lee.fielding@manchester.ac.uk (L.A.F.).
*E-mail s.p.armes@sheffield.ac.uk (S.P.A.).

Present Address
B.A.: Department of Chemistry, Imperial College London, South Kensington Campus, London SW7 2AZ, UK.

Notes
The authors declare no competing financial interest.

REFERENCES

(1) Napper, D. H. Steric stabilization. *J. Colloid Interface Sci.* **1977**, 58 (2), 390−407.

(2) Napper, D. H. *Polymeric Stabilization of Colloidal Dispersions*; Academic Press: London, 1983.

(3) Hunter, R. J. *Foundations of Colloid Science*; Oxford University Press: Oxford, 2000.

(4) Lascelles, S. F.; Malet, F.; Mayada, R.; Billingham, N. C.; Armes, S. P. Latex syntheses using novel tertiary amine methacrylate-based macromonomers prepared by oxyanionic polymerization. *Macromolecules* **1999**, 32 (8), 2462−2471.

(5) Almog, Y.; Reich, S.; Levy, M. Monodisperse polymeric spheres in the micron size range by a single step process. *Br. Polym. J.* **1982**, 14 (4), 131−136.

(6) Ober, C. K.; Lok, K. P.; Hair, M. L. Monodispersed, micron-sized polystyrene particles by dispersion polymerization. *J. Polym. Sci., Polym. Lett. Ed.* **1985**, 23 (2), 103−108.

(7) Tseng, C. M.; Lu, Y. Y.; Elaasser, M. S.; Vanderhoff, J. W. Uniform polymer particles by dispersion polymerization in alcohol. *J. Polym. Sci., Part A: Polym. Chem.* **1986**, 24 (11), 2995−3007.

(8) Paine, A. J.; Luymes, W.; McNulty, J. Dispersion polymerization of styrene in polar-solvents 0.6. Influence of reaction parameters on particle-size and molecular-weight in poly(n-vinylpyrrolidone)-stabilized reactions. *Macromolecules* **1990**, 23 (12), 3104−3109.

(9) Shen, S.; Sudol, E. D.; Elaasser, M. S. Control of particle-size in dispersion polymerization of methyl-methacrylate. *J. Polym. Sci., Part A: Polym. Chem.* **1993**, 31 (6), 1393−1402.

(10) Baines, F. L.; Dionisio, S.; Billingham, N. C.; Armes, S. P. Use of block copolymer stabilizers for the dispersion polymerization of styrene in alcoholic media. *Macromolecules* **1996**, 29 (9), 3096−3102.

(11) Ali, A. M. I.; Pareek, P.; Sewell, L.; Schmid, A.; Fujii, S.; Armes, S. P.; Shirley, I. M. Synthesis of poly(2-hydroxypropyl methacrylate) latex particles via aqueous dispersion polymerization. *Soft Matter* **2007**, 3 (8), 1003−1013.

(12) Barrett, K. E. J.; Thomas, H. R. Kinetics of dispersion polymerization of soluble monomers.I. Methyl methacrylate. *J. Polym. Sci., Part A-1: Polym. Chem.* **1969**, 7 (9PA1), 2621−2650.

(13) Dawkins, J. V.; Taylor, G. Non-aqueous poly(methyl methacrylate) dispersions - radical dispersion polymerization in the presence of ab block copolymers of polystyrene and poly(dimethyl siloxane). *Polymer* **1979**, 20 (5), 599−604.

(14) Antl, L.; Goodwin, J. W.; Hill, R. D.; Ottewill, R. H.; Owens, S. M.; Papworth, S.; Waters, J. A. The preparation of poly(methyl

methacrylate) lattices in nonaqueous media. *Colloids Surf.* **1986**, *17* (1), 67–78.

(15) Stejskal, J.; Kratochvil, P.; Konak, C. Structural parameters of spherical-particles prepared by dispersion polymerization of methyl-methacrylate. *Polymer* **1991**, *32* (13), 2435–2442.

(16) Jenkins, A. D.; Maxfield, D.; Dossantos, C. G.; Walton, D. R. M.; Stejskal, J.; Kratochvil, P. Enolate-initiated dispersion polymerization. *Makromol. Chem., Rapid Commun.* **1992**, *13* (1), 61–63.

(17) Awan, M. A.; Dimonie, V. L.; ElAasser, M. S. Anionic dispersion polymerization of styrene 0.2. Mechanism of particle formation. *J. Polym. Sci., Part A: Polym. Chem.* **1996**, *34* (13), 2651–2664.

(18) Awan, M. A.; Dimonie, V. L.; ElAasser, M. S. Anionic dispersion polymerization of styrene 0.1. Investigation of parameters for preparation of uniform micron-size polystyrene particles with narrow molecular weight distribution. *J. Polym. Sci., Part A: Polym. Chem.* **1996**, *34* (13), 2633–2649.

(19) Richez, A. P.; Yow, H. N.; Biggs, S.; Cayre, O. J. Dispersion polymerization in non-polar solvent: Evolution toward emerging applications. *Prog. Polym. Sci.* **2013**, *38* (6), 897–931.

(20) Fielding, L. A.; Derry, M. J.; Ladmiral, V.; Rosselgong, J.; Rodrigues, A. M.; Ratcliffe, L. P. D.; Sugihara, S.; Armes, S. P. RAFT dispersion polymerization in non-polar solvents: facile production of block copolymer spheres, worms and vesicles in n-alkanes. *Chemical Science* **2013**, *4* (5), 2081–2087.

(21) Richez, A. P.; Farrand, L.; Goulding, M.; Wilson, J. H.; Lawson, S.; Biggs, S.; Cayre, O. J. Dispersion Polymerization of Poly-(dimethylsiloxane)-Stabilized Polymer Particles from Radical Dispersion Polymerization in Nonpolar Solvent: Influence of Stabilizer Properties and Monomer Type. *Langmuir* **2014**, *30* (5), 1220–1228.

(22) DeSimone, J. M.; Maury, E. E.; Menceloglu, Y. Z.; McClain, J. B.; Romack, T. J.; Combes, J. R. Dispersion polymerizations in supercritical carbon-dioxide. *Science* **1994**, *265* (5170), 356–359.

(23) Hsiao, Y. L.; Maury, E. E.; DeSimone, J. M.; Mawson, S.; Johnston, K. P. Dispersion polymerization of methyl-methacrylate stabilized with poly(1,1-dihydroperfluorooctyl acrylate) in supercritical carbon-dioxide. *Macromolecules* **1995**, *28* (24), 8159–8166.

(24) Shaffer, K. A.; Jones, T. A.; Canelas, D. A.; DeSimone, J. M.; Wilkinson, S. P. Dispersion polymerizations in carbon dioxide using siloxane-based stabilizers. *Macromolecules* **1996**, *29* (7), 2704–2706.

(25) Giles, M. R.; Griffiths, R. M. T.; Aguiar-Ricardo, A.; Silva, M.; Howdle, S. M. Fluorinated graft stabilizers for polymerization in supercritical carbon dioxide: The effect of stabilizer architecture. *Macromolecules* **2001**, *34* (1), 20–25.

(26) Wang, W. X.; Griffiths, R. M. T.; Naylor, A.; Giles, M. R.; Irvine, D. J.; Howdle, S. M. Preparation of cross-linked microparticles of poly(glycidyl methacrylate) by dispersion polymerization of glycidyl methacrylate using a PDMS macromonomer as stabilizer in supercritical carbon dioxide. *Polymer* **2002**, *43* (25), 6653–6659.

(27) Lee, H.; Terry, E.; Zong, M.; Arrowsmith, N.; Perrier, S.; Thurecht, K. J.; Howdle, S. M. Successful dispersion polymerization in supercritical CO₂ using polyvinylalkylate hydrocarbon surfactants synthesized and anchored via RAFT. *J. Am. Chem. Soc.* **2008**, *130* (37), 12242–12243.

(28) Minami, H.; Yoshida, K.; Okubo, M. Preparation of polystyrene particles by dispersion polymerization in an ionic liquid. *Macromol. Rapid Commun.* **2008**, *29* (7), 567–572.

(29) Minami, H.; Kimura, A.; Kinoshita, K.; Okubo, M. Preparation of poly(acrylic acid) particles by dispersion polymerization in an ionic liquid. *Langmuir* **2010**, *26* (9), 6303–6307.

(30) Barrett, K. E. J. *Dispersion Polymerization in Organic Media*; Wiley: 1974.

(31) Cesarano, J.; Aksay, I. A. Processing of highly concentrated aqueous alpha-alumina suspensions stabilized with poly-electrolytes. *J. Am. Ceram. Soc.* **1988**, *71* (12), 1062–1067.

(32) Allami, H. S.; Billingham, N. C.; Calvert, P. D. Controlled structure methacrylic copolymers as dispersants for ceramics processing. *Chem. Mater.* **1992**, *4* (6), 1200–1207.

(33) Chen, Z. C.; Ring, T. A.; Lemaitre, J. Stabilization and processing of aqueous BaTiO3 suspension with polyacrylic-acid. *J. Am. Ceram. Soc.* **1992**, *75* (12), 3201–3208.

(34) Bhattacharjee, S.; Paria, M. K.; Maiti, H. S. Polyvinyl butyral as a dispersant for barium-titanate in a nonaqueous suspension. *J. Mater. Sci.* **1993**, *28* (23), 6490–6495.

(35) Vamvakaki, M.; Billingham, N. C.; Armes, S. P.; Watts, J. F.; Greaves, S. J. Controlled structure copolymers for the dispersion of highperformance ceramics in aqueous media. *J. Mater. Chem.* **2001**, *11* (10), 2437–2444.

(36) Magdassi, S.; Bassa, A.; Vinetsky, Y.; Kamyshny, A. Silver nanoparticles as pigments for water-based ink-jet inks. *Chem. Mater.* **2003**, *15* (11), 2208–2217.

(37) Won, Y. Y.; Meeker, S. P.; Trappe, V.; Weitz, D. A.; Diggs, N. Z.; Emert, J. I. Effect of temperature on carbon-black agglomeration in hydrocarbon liquid with adsorbed dispersant. *Langmuir* **2005**, *21* (3), 924–932.

(38) Growney, D. J.; Mykhaylyk, O. O.; Armes, S. P. Micellization and adsorption behavior of a near-monodisperse polystyrene-based diblock copolymer in nonpolar media. *Langmuir* **2014**, *30* (21), 6047–6056.

(39) Growney, D. J.; Mykhaylyk, O. O.; Derouineau, T.; Fielding, L. A.; Smith, A. J.; Aragrag, N.; Lamb, G. D.; Armes, S. P. Star diblock copolymer concentration dictates the degree of dispersion of carbon black particles in nonpolar media: Bridging flocculation versus steric stabilization. *Macromolecules* **2015**, *48* (11), 3691–3704.

(40) Stolnik, S.; Dunn, S. E.; Garnett, M. C.; Davies, M. C.; Coombes, A. G. A.; Taylor, D. C.; Irving, M. P.; Purkiss, S. C.; Tadros, T. F.; Davis, S. S.; Illum, L. Surface modification of poly(lactide-co-glycolide) nanospheres by biodegradable poly(lactide)-poly(ethylene glycol) copolymers. *Pharm. Res.* **1994**, *11* (12), 1800–1808.

(41) Feng, W.; Zhu, S. P.; Ishihara, K.; Brash, J. L. Adsorption of fibrinogen and lysozyme on silicon grafted with poly(2-methacryloyloxyethyl phosphorylcholine) via surface-initiated atom transfer radical polymerization. *Langmuir* **2005**, *21* (13), 5980–5987.

(42) Feng, W.; Brash, J. L.; Zhu, S. P. Non-biofouling materials prepared by atom transfer radical polymerization grafting of 2-methacryloloxyethyl phosphorylcholine: Separate effects of graft density and chain length on protein repulsion. *Biomaterials* **2006**, *27* (6), 847–855.

(43) Jiang, S. Y.; Cao, Z. Q. Ultralow-fouling, functionalizable, and hydrolyzable zwitterionic materials and their derivatives for biological applications. *Adv. Mater.* **2010**, *22* (9), 920–932.

(44) Zhang, L.; Cao, Z.; Bai, T.; Carr, L.; Ella-Menye, J.-R.; Irvin, C.; Ratner, B. D.; Jiang, S. Zwitterionic hydrogels implanted in mice resist the foreign-body reaction. *Nat. Biotechnol.* **2013**, *31* (6), 553–556.

(45) Alswieleh, A. M.; Cheng, N.; Canton, I.; Ustbas, B.; Xue, X.; Ladmiral, V.; Xia, S.; Ducker, R. E.; El Zubir, O.; Cartron, M. L.; Hunter, C. N.; Leggett, G. J.; Armes, S. P. Zwitterionic poly(amino acid methacrylate) brushes. *J. Am. Chem. Soc.* **2014**, *136* (26), 9404–9413.

(46) Reed, K. M.; Borovicka, J.; Horozov, T. S.; Paunov, V. N.; Thompson, K. L.; Walsh, A.; Armes, S. P. Adsorption of sterically stabilized latex particles at liquid surfaces: Effects of steric stabilizer surface coverage, particle size, and chain length on particle wettability. *Langmuir* **2012**, *28* (18), 7291–7298.

(47) Amalvy, J. I.; Unali, G. F.; Li, Y.; Granger-Bevan, S.; Armes, S. P.; Binks, B. P.; Rodrigues, J. A.; Whitby, C. P. Synthesis of sterically stabilized polystyrene latex particles using cationic block copolymers and macromonomers and their application as stimulus-responsive particulate emulsifiers for oil-in-water emulsions. *Langmuir* **2004**, *20* (11), 4345–4354.

(48) Detloff, T.; Sobisch, T.; Lerche, D. Particle size distribution by space or time dependent extinction profiles obtained by analytical centrifugation (concentrated systems). *Powder Technol.* **2007**, *174* (1–2), 50–55.

(49) Planken, K. L.; Cölfen, H. Analytical ultracentrifugation of colloids. *Nanoscale* **2010**, *2* (10), 1849–1869.

(50) Fielding, L. A.; Mykhaylyk, O. O.; Armes, S. P.; Fowler, P. W.; Mittal, V.; Fitzpatrick, S. Correcting for a density distribution: Particle size analysis of core−shell nanocomposite particles using disk centrifuge photosedimentometry. *Langmuir* **2012**, *28* (5), 2536−2544.

(51) Weiss, A.; Dingenouts, N.; Ballauff, M.; Senff, H.; Richtering, W. Comparison of the Effective Radius of Sterically Stabilized Latex Particles Determined by Small-Angle X-ray Scattering and by Zero Shear Viscosity. *Langmuir* **1998**, *14* (18), 5083−5087.

(52) Seelenmeyer, S.; Ballauff, M. Analysis of surfactants adsorbed onto the surface of latex particles by small-angle X-ray scattering. *Langmuir* **2000**, *16* (9), 4094−4099.

(53) Cohen Stuart, M. A.; Cosgrove, T.; Vincent, B. Experimental aspects of polymer adsorption at solid-solution interfaces. *Adv. Colloid Interface Sci.* **1985**, *24* (2−3), 143−239.

(54) Ferguson, C. J.; Hughes, R. J.; Nguyen, D.; Pham, B. T. T.; Gilbert, R. G.; Serelis, A. K.; Such, C. H.; Hawkett, B. S. Ab initio emulsion polymerization by RAFT-controlled self-assembly. *Macromolecules* **2005**, *38* (6), 2191−2204.

(55) An, Z.; Shi, Q.; Tang, W.; Tsung, C.-K.; Hawker, C. J.; Stucky, G. D. Facile RAFT precipitation polymerization for the microwave-assisted synthesis of well-defined, double hydrophilic block copolymers and nanostructured hydrogels. *J. Am. Chem. Soc.* **2007**, *129* (46), 14493−14499.

(56) Wan, W.-M.; Hong, C.-Y.; Pan, C.-Y. One-pot synthesis of nanomaterials via RAFT polymerization induced self-assembly and morphology transition. *Chem. Commun.* **2009**, *39*, 5883−5885.

(57) Rieger, J.; Grazon, C.; Charleux, B.; Alaimo, D.; Jerome, C. Pegylated thermally responsive block copolymer micelles and nanogels via in situ raft aqueous dispersion polymerization. *J. Polym. Sci., Part A: Polym. Chem.* **2009**, *47* (9), 2373−2390.

(58) Rieger, J.; Zhang, W.; Stoffelbach, F.; Charleux, B. Surfactant-free RAFT emulsion polymerization using poly(N,N-dimethylacrylamide) trithiocarbonate macromolecular chain transfer agents. *Macromolecules* **2010**, *43* (15), 6302−6310.

(59) Chaduc, I.; Zhang, W.; Rieger, J.; Lansalot, M.; D'Agosto, F.; Charleux, B. Amphiphilic block copolymers from a direct and one-pot raft synthesis in water. *Macromol. Rapid Commun.* **2011**, *32* (16), 1270−1276.

(60) Chaduc, I.; Girod, M.; Antoine, R.; Charleux, B.; D'Agosto, F.; Lansalot, M. Batch emulsion polymerization mediated by poly-(methacrylic acid) macroraft agents: One-pot synthesis of self-stabilized particles. *Macromolecules* **2012**, *45* (15), 5881−5893.

(61) Charleux, B.; Delaittre, G.; Rieger, J.; D'Agosto, F. Polymerization-induced self-assembly: From soluble macromolecules to block copolymer nano-objects in one step. *Macromolecules* **2012**, *45* (17), 6753−6765.

(62) Semsarilar, M.; Jones, E. R.; Blanazs, A.; Armes, S. P. Efficient synthesis of sterically-stabilized nano-objects via RAFT dispersion polymerization of benzyl methacrylate in alcoholic media. *Adv. Mater.* **2012**, *24* (25), 3378−3382.

(63) Warren, N. J.; Armes, S. P. Polymerization-induced self-assembly of block copolymer nano-objects via RAFT aqueous dispersion polymerization. *J. Am. Chem. Soc.* **2014**, *136* (29), 10174−10185.

(64) Cunningham, V. J.; Alswieleh, A. M.; Thompson, K. L.; Williams, M.; Leggett, G. J.; Armes, S. P.; Musa, O. M. Poly(glycerol monomethacrylate)-poly(benzyl methacrylate) diblock copolymer nanoparticles via RAFT emulsion polymerization: Synthesis, characterization, and interfacial activity. *Macromolecules* **2014**, *47* (16), 5613−5623.

(65) Pei, Y.; Dharsana, N. C.; Van Hensbergen, J. A.; Burford, R. P.; Roth, P. J.; Lowe, A. B. RAFT dispersion polymerization of 3-phenylpropyl methacrylate with poly 2-(dimethylamino)ethyl methacrylate macro-CTAs in ethanol and associated thermoreversible polymorphism. *Soft Matter* **2014**, *10* (31), 5787−5796.

(66) Pei, Y.; Lowe, A. B. Polymerization-induced self-assembly: ethanolic RAFT dispersion polymerization of 2-phenylethyl methacrylate. *Polym. Chem.* **2014**, *5* (7), 2342−2351.

(67) Pei, Y.; Thurairajah, L.; Sugita, O. R.; Lowe, A. B. RAFT dispersion polymerization in nonpolar media: Polymerization of 3-phenylpropyl methacrylate in n-tetradecane with poly(stearyl methacrylate) homopolymers as macro chain transfer agents. *Macromolecules* **2014**, *48* (1), 236−244.

(68) Fielding, L. A.; Lane, J. A.; Derry, M. J.; Mykhaylyk, O. O.; Armes, S. P. Thermo-responsive diblock copolymer worm gels in non-polar solvents. *J. Am. Chem. Soc.* **2014**, *136* (15), 5790−5798.

(69) Derry, M. J.; Fielding, L. A.; Armes, S. P. Industrially-relevant polymerization-induced self-assembly formulations in non-polar solvents: RAFT dispersion polymerization of benzyl methacrylate. *Polym. Chem.* **2015**, *6* (16), 3054−3062.

(70) Derry, M. J.; Fielding, L. A.; Armes, S. P. Polymerization-induced self-assembly of block copolymer nanoparticles via RAFT non-aqueous dispersion polymerization. *Prog. Polym. Sci.* **2016**, *52*, 1−18.

(71) Ilavsky, J.; Jemian, P. R. Irena: tool suite for modeling and analysis of small-angle scattering. *J. Appl. Crystallogr.* **2009**, *42*, 347−353.

(72) Brandup, J.; Immergut, E. H. *Polymer Handbook*; John Wiley & Sons: New York, 1975.

(73) Smallwood, I. M. In *Handbook of Organic Solvent Properties*; Smallwood, I. M., Ed.; Butterworth-Heinemann: Oxford, 1996; pp 245−247.

(74) Semsarilar, M.; Jones, E. R.; Armes, S. P. Comparison of pseudo-living character of RAFT polymerizations conducted under homogeneous and heterogeneous conditions. *Polym. Chem.* **2014**, *5* (1), 195−203.

(75) Blanazs, A.; Verber, R.; Mykhaylyk, O. O.; Ryan, A. J.; Heath, J. Z.; Douglas, C. W. I.; Armes, S. P. Sterilizable gels from thermoresponsive block copolymer worms. *J. Am. Chem. Soc.* **2012**, *134* (23), 9741−9748.

(76) Ratcliffe, L. P. D.; Blanazs, A.; Williams, C. N.; Brown, S. L.; Armes, S. P. RAFT polymerization of hydroxy-functional methacrylic monomers under heterogeneous conditions: effect of varying the core-forming block. *Polym. Chem.* **2014**, *5* (11), 3643−3655.

(77) Pedersen, J. S.; Gerstenberg, M. C. The structure of P85 Pluronic block copolymer micelles determined by small-angle neutron scattering. *Colloids Surf., A* **2003**, *213* (2−3), 175−187.

(78) Cunningham, V. J.; Ratcliffe, L. P. D.; Blanazs, A.; Warren, N. J.; Smith, A. J.; Mykhaylyk, O. O.; Armes, S. P. Tuning the critical gelation temperature of thermo-responsive diblock copolymer worm gels. *Polym. Chem.* **2014**, *5* (21), 6307−6317.

(79) Fetters, L. J.; Lohse, D. J.; Colby, R. H. In *Physical Properties of Polymers Handbook*, Mark, J., Ed.; Springer: New York, 2007; pp 447−454.

(80) Peng, H.; Thurecht, K. J.; Blakey, I.; Taran, E.; Whittaker, A. K. Effect of solvent quality on the solution properties of assemblies of partially fluorinated amphiphilic diblock copolymers. *Macromolecules* **2012**, *45* (21), 8681−8690.

(81) Zinn, T.; Willner, L.; Lund, R.; Pipich, V.; Appavou, M. S.; Richter, D. Surfactant or block copolymer micelles? Structural properties of a series of well-defined n-alkyl-PEO micelles in water studied by SANS. *Soft Matter* **2014**, *10* (28), 5212−5220.

(82) Dupin, D.; Fujii, S.; Armes, S. P.; Reeve, P.; Baxter, S. M. Efficient synthesis of sterically stabilized pH-responsive microgels of controllable particle diameter by emulsion polymerization. *Langmuir* **2006**, *22* (7), 3381−3387.

(83) Dupin, D.; Howse, J. R.; Armes, S. P.; Randall, D. P. Preparation of stable foams using sterically stabilized pH-responsive latexes synthesized by emulsion polymerization. *J. Mater. Chem.* **2008**, *18* (5), 545−552.

(84) Walczyk, D.; Bombelli, F. B.; Monopoli, M. P.; Lynch, I.; Dawson, K. A. What the cell "sees" in bionanoscience. *J. Am. Chem. Soc.* **2010**, *132* (16), 5761−5768.

(85) Bucsi, A.; Forcada, J.; Gibanel, S.; Heroguez, V.; Fontanille, M.; Gnanou, Y. Monodisperse polystyrene latex particles functionalized by the macromonomer technique. *Macromolecules* **1998**, *31* (7), 2087−2097.

(86) Verdurmen, E. M.; Albers, J. G.; German, A. L. Polybutadiene latex particle-size distribution analysis utilizing a disk centrifuge. *Colloid Polym. Sci.* **1994**, *272* (1), 57−63.

(87) Elizalde, O.; Leal, G. P.; Leiza, J. R. Particle size distribution measurements of polymeric dispersions: A comparative study. *Part. Part. Syst. Charact.* **2000**, *17* (5−6), 236−243.

(88) Thomas, J. C.; Middelberg, A. P. J.; Hamel, J. F.; Snoswell, M. A. High-resolution particle-size analysis in biotechnology process-control. *Biotechnol. Prog.* **1991**, *7* (4), 377−379.

(89) Middelberg, A. P. J.; Bogle, I. D. L.; Snoswell, M. A. Sizing biological samples by photosedimentation techniques. *Biotechnol. Prog.* **1990**, *6* (4), 255−261.

(90) Bondoc, L. L.; Fitzpatrick, S. Size distribution analysis of recombinant adenovirus using disc centrifugation. *J. Ind. Microbiol. Biotechnol.* **1998**, *20* (6), 317−322.

(91) Neumann, A.; Hoyer, W.; Wolff, M. W.; Reichl, U.; Pfitzner, A.; Roth, B. New method for density determination of nanoparticles using a CPS disc centrifuge. *Colloids Surf., B* **2013**, *104* (0), 27−31.

(92) Fielding, L. A.; Armes, S. P.; Staniland, P.; Sayer, R.; Tooley, I. Physical adsorption of anisotropic titania nanoparticles onto poly(2-vinylpyridine) latex and characterisation of the resulting nano-composite particles. *J. Colloid Interface Sci.* **2014**, *426*, 170−180.

(93) Fielding, L. A.; Mykhaylyk, O. O.; Schmid, A.; Pontoni, D.; Armes, S. P.; Fowler, P. W. Visible Mie scattering from hollow silica particles with particulate shells. *Chem. Mater.* **2014**, *26* (2), 1270−1277.

(94) Fielding, L. A.; Tonnar, J.; Armes, S. P. All-acrylic film-forming colloidal polymer/silica nanocomposite particles prepared by aqueous emulsion polymerization. *Langmuir* **2011**, *27* (17), 11129−11144.

(95) Balmer, J. A.; Le Cunff, E. C.; Armes, S. P.; Murray, M. W.; Murray, K. A.; Williams, N. S. J. When does silica exchange occur between vinyl polymer-silica nanocomposite particles and sterically stabilized latexes? *Langmuir* **2010**, *26* (16), 13662−13671.

(96) Gill, M.; Armes, S. P.; Fairhurst, D.; Emmett, S. N.; Idzorek, G.; Pigott, T. Particle-size distributions of polyaniline silica colloidal composites. *Langmuir* **1992**, *8* (9), 2178−2182.

(97) Han, M. G.; Armes, S. P. Synthesis of poly(3,4-ethyl-enedioxythiophene)/silica colloidal nanocomposites. *Langmuir* **2003**, *19* (11), 4523−4526.

(98) Maeda, S.; Armes, S. P. Preparation and characterization of novel polypyrrole-silica colloidal nanocomposites. *J. Mater. Chem.* **1994**, *4* (6), 935−942.

(99) Maeda, S.; Ames, S. P. Preparation and characterization of polypyrrole tin(IV) oxide nanocomposite colloids. *Chem. Mater.* **1995**, *7* (1), 171−178.

(100) Percy, M. J.; Barthet, C.; Lobb, J. C.; Khan, M. A.; Lascelles, S. F.; Vamvakaki, M.; Armes, S. P. Synthesis and characterization of vinyl polymer-silica colloidal nanocomposites. *Langmuir* **2000**, *16* (17), 6913−6920.

(101) Monopoli, M. P.; Walczyk, D.; Campbell, A.; Elia, G.; Lynch, I.; Baldelli Bombelli, F.; Dawson, K. A. Physical−chemical aspects of protein corona: Relevance to in vitro and in vivo biological impacts of nanoparticles. *J. Am. Chem. Soc.* **2011**, *133* (8), 2525−2534.

(102) Nadler, M.; Mahrholz, T.; Riedel, U.; Schilde, C.; Kwade, A. Preparation of colloidal carbon nanotube dispersions and their characterisation using a disc centrifuge. *Carbon* **2008**, *46* (11), 1384−1392.

(103) Zerrouki, D.; Rotenberg, B.; Abramson, S.; Baudry, J.; Goubault, C.; Leal-Calderon, F.; Pine, D. J.; Bibette, M. Preparation of doublet, triangular, and tetrahedral colloidal clusters by controlled emulsification. *Langmuir* **2006**, *22* (1), 57−62.

(104) Colard, C. A. L.; Teixeira, R. F. A.; Bon, S. A. F. Unraveling mechanistic events in solids-stabilized emulsion polymerization by monitoring the concentration of nanoparticles in the water phase. *Langmuir* **2010**, *26* (11), 7915−7921.

(105) Subramanian, R.; Zhu, S.; Pelton, R. H. Synthesis and flocculation performance of graft and random copolymer microgels of acrylamide and diallyldimethylammonium chloride. *Colloid Polym. Sci.* **1999**, *277* (10), 939−946.

(106) Ramirez-Garcia, S.; Chen, L.; Morris, M. A.; Dawson, K. A. A new methodology for studying nanoparticle interactions in biological systems: Dispersing titania in biocompatible media using chemical stabilisers. *Nanoscale* **2011**, *3* (11), 4617−4624.

(107) Kamiti, M.; Boldridge, D.; Ndoping, L. M.; Remsen, E. E. Simultaneous absolute determination of particle size and effective density of submicron colloids by disc centrifuge photosedimentometry. *Anal. Chem.* **2012**, *84* (24), 10526−10530.

(108) Kohler, J. M.; Wagner, J.; Albert, J. Formation of isolated and clustered Au nanoparticles in the presence of polyelectrolyte molecules using a flow-through Si chip reactor. *J. Mater. Chem.* **2005**, *15* (19), 1924−1930.

(109) Krpetic, Z.; Porta, F.; Caneva, E.; Dal Santo, V.; Scari, G. Phagocytosis of biocompatible gold nanoparticles. *Langmuir* **2010**, *26* (18), 14799−14805.

(110) Lowe, A. B.; Sumerlin, B. S.; Donovan, M. S.; McCormick, C. L. Facile preparation of transition metal nanoparticles stabilized by well-defined (Co)polymers synthesized via aqueous reversible addition-fragmentation chain transfer polymerization. *J. Am. Chem. Soc.* **2002**, *124* (39), 11562−11563.

(111) Daniel, M.-C.; Astruc, D. Gold nanoparticles: Assembly, supramolecular chemistry, quantum-size-related properties, and applications toward biology, catalysis, and nanotechnology. *Chem. Rev.* **2004**, *104* (1), 293−346.

(112) Barrow, M.; Taylor, A.; Nieves, D. J.; Bogart, L. K.; Mandal, P.; Collins, C. M.; Moore, L. R.; Chalmers, J. J.; Levy, R.; Williams, S. R.; Murray, P.; Rosseinsky, M. J.; Adams, D. J. Tailoring the surface charge of dextran-based polymer coated SPIONs for modulated stem cell uptake and MRI contrast. *Biomater. Sci.* **2015**, *3* (4), 608−616.

(113) Sakulkhu, U.; Mahmoudi, M.; Maurizi, L.; Coullerez, G.; Hofmann-Amtenbrink, M.; Vries, M.; Motazacker, M.; Rezaee, F.; Hofmann, H. Significance of surface charge and shell material of superparamagnetic iron oxide nanoparticle (SPION) based core/shell nanoparticles on the composition of the protein corona. *Biomater. Sci.* **2015**, *3* (2), 265−278.

(114) Yuan, J. J.; Armes, S. P.; Takabayashi, Y.; Prassides, K.; Leite, C. A. P.; Galembeck, F.; Lewis, A. L. Synthesis of biocompatible poly[2-(methacryloyloxy)ethyl phosphorylcholine]-coated magnetite nanoparticles. *Langmuir* **2006**, *22* (26), 10989−10993.

(115) Harris, L. A.; Goff, J. D.; Carmichael, A. Y.; Riffle, J. S.; Harburn, J. J., St; St. Pierre, T. G.; Saunders, M. Magnetite nanoparticle dispersions stabilized with triblock copolymers. *Chem. Mater.* **2003**, *15* (6), 1367−1377.

(116) Lee, H.; Lee, E.; Kim, D. K.; Jang, N. K.; Jeong, Y. Y.; Jon, S. Antibiofouling polymer-coated superparamagnetic iron oxide nano-particles as potential magnetic resonance contrast agents for in vivo cancer imaging. *J. Am. Chem. Soc.* **2006**, *128* (22), 7383−7389.